HAL
open science

Crustal accretion at a sedimented spreading center in the Andaman Sea

Aurélie Jourdain, Satish Singh, Javier Escartin, Yann Klinger, K.A. Kamesh Raju, J. Mcardle

To cite this version:

Aurélie Jourdain, Satish Singh, Javier Escartin, Yann Klinger, K.A. Kamesh Raju, et al.. Crustal accretion at a sedimented spreading center in the Andaman Sea. Geology, 2016, 44 (5), pp.351-354. 10.1130/G37537.1 . hal-02330296

HAL Id: hal-02330296

https://hal.science/hal-02330296v1

Submitted on 19 Oct 2021

HAL is a multi-disciplinary open access archive for the deposit and dissemination of scientific research documents, whether they are published or not. The documents may come from teaching and research institutions in France or abroad, or from public or private research centers.

L'archive ouverte pluridisciplinaire **HAL**, est destinée au dépôt et à la diffusion de documents scientifiques de niveau recherche, publiés ou non, émanant des établissements d'enseignement et de recherche français ou étrangers, des laboratoires publics ou privés.

Crustal accretion at a sedimented spreading center in the Andaman Sea

Aurélie Jourdain[1], Satish C. Singh[1], Javier Escartin[1], Yann Klinger[1], K. A. Kamesh Raju[2], J. McArdle[3]

[1]*Institut de Physique du Globe de Paris, Sorbonne Paris Cité, UMR7154-CNRS, 1 rue Jussieu, 78238 Paris Cedex 05, France*

[2]*CSIR-National Institute of Oceanography, Dona Paula, Goa 403 004, India*

[3]*Petroleum Geo-services, 111 Somerset Road, Singapore 238164*

ABSTRACT

The combination of magmatic, tectonic, and hydrothermal processes that from the oceanic crust, relatively well understood along mid-ocean spreading centers, is strongly modified at sedimented spreading centers, which are still poorly understood owing to the lack of good crustal images. Here we present high-resolution deep seismic reflection images across the sedimented slow-spreading Andaman Sea spreading center that shows several sub-horizontal sills injected within the sedimentary strata beneath the axial graben. Below this sill-sediment sequence we observe reverse polarity reflections within the igneous crust, indicative of the existence of axial magma lenses (AMLs) at different depths. This results in a heterogeneous upper crust that incorporates metamorphosed sediments. The faults within the axial valley are steeply dipping (65-75º) and are in a stair-cased pattern. Their base coincides with a shallow dipping (30º) reflection, possibly defining the spreading axis morphology, controlled by the AMLs. We propose that as the sill-sediment sequences move away from the axial graben, they

are rotated and buried due to subsidence and faulting, forming the upper oceanic crust. The Moho reflections are observed along a significant part of the profiles, allowing the characterization of the whole crustal structure. We find that the upper oceanic crust is formed by a combination of sill-sediment sequence, followed by a thick gabbroic lower crust with some sediment along faults, with a mantle transition containing dunite lenses near the Moho.

INTRODUCTION AND SETTING

The oceanic crust forms at mid-ocean spreading centers by a combination of magmatic, tectonic, and hydrothermal processes that are relatively well studied along both fast- and slow-spreading mid-ocean ridges. However, sediments can drown spreading centers in the vicinity of continents or during the early stages of continental rifting and oceanization, as observed in the Guaymas Basin (Lizarralde et al., 2011; Kluesner et al, 2014), northern Juan de Fuca Ridge (Davis and Becker 2002), and Mohns Ridge (Bruvoll et al., 2009). These sediments capping spreading centers can significantly modify the axial thermal regime and fluid circulation, and therefore the accretion processes (melt emplacement, faulting), and also the overall lithospheric structure and composition. To better understand the impact of sedimentation on crustal accretion, we present the first whole-crust, high-resolution multichannel seismic reflection images across the sedimented Andaman Sea Spreading Center (ASSC). The unprecedented resolution of these data allow us to image clearly the interactions of sedimentation and accretion, and to propose a general model of lithospheric formation and whole-crust structure at sedimented mid-ocean ridges.

The ASSC back-arc spreading center separates the Burmese sliver plate to the northwest from the Sunda plate (Eurasia) to the southwest (Fig. 1A) (Curray et al., 1979; Kamesh Raju et al., 2004). It connects the northern Sagaing strike-slip fault with the southern Andaman-Nicobar and Sumatra faults (Sieh and Natawidjaja, 2000), which result from strain partitioning from the oblique Indian plate subduction beneath the Sunda plate (Fitch, 1972). Based on magnetic anomalies on the westernmost non-sedimented segment, ASSC spreading initiated 4 Ma ago at a full rate of 16 mm/yr, speeding to 38 mm/yr 2 Ma ago (Kamesh Raju et al., 2004).

Most of the Andaman Sea basin is sedimented and flat lying at 3000 m water depth. The ASSC, at the center of the basin, displays a ~12 km wide axial valley, and an also flat-lying rift valley floor at 3600 m water depth (Fig. 1B), infilled by sediments from the Irrawaddy river basin in Myanmar (Fig. 1A) (Curray et al., 1979). This sedimented axial graben is bound by normal faults and tilted fault blocks, reminiscent of the structure found at slow spreading ridges (e.g., Needham and Francheteau, 1974).

SEISMIC DATA

The seismic reflection data were acquired by Petroleum Geo-Services (PGS) in 2008 with a 6400 cubic inch air gun array and recorded by an 8-km long streamer with a group spacing of 12.5 m. The air gun and the streamer were towed at 8 m and 10 m below the sea surface respectively, with a 25 m shot interval and a 9 s record length. Data were processed using a conventional time migration technique, which includes swell noise removal, trace editing to remove noisy traces, common midpoint binning, velocity analysis, upper mute, and stacking. Stacked data were

migrated using a post-stack Kirchhoff migration technique. PGS provided the final migrated data and root mean square (RMS) velocities every 1 km (160 CMP), and no pre-stack data were available for our study. Here we present two N-S profiles crossing the sedimented segment of the ASSC and spaced ~40 km (Fig. 1B).

Figure 2 shows the interpreted seismic time sections along the two profiles that cross the rift valley; un-interpreted images are shown in Figure S1. Although the profiles are N-S, 25° NE off the orthogonal to the spreading axis, symmetry of structures on either side of the axial graben are clear, and show as well as the thick sediments filling the axial valley, and numerous faults penetrating down 2-2.5 s. The 7.5 s deep reflection is the Moho which appears intermittently along both profiles.

In the absence of seismic refraction studies, we converted RMS velocities into interval velocities, laterally smoothed to obtain a continuous velocity and seismic image. Although the RMS-derived interval velocities are less accurate than those from refraction data, they provide insight into crustal structure. The P-wave velocity increases from 1.6 km/s near the seafloor to 3.0 km/s at the sedimentary sequence bottom/base? (Fig. S2), which combined with the linear seismic reflections suggest the presence of sedimentation layering. The alternating highly reflective and transparent layers within the sedimentary column could correspond to sediment deposits recording climate variability (Kluesner et al., 2014). Further below velocity increases sharply to 4.5 km/s within a 0.6 s thick zone, associated with a layer displaying numerous bright reflections. Deeper and up to Moho, the reflective features are sparse but mostly steeply dipping. Lacking seismic reflectors, the seismic velocity in this region is poorly constrained.

INTERPRETATION OF SEISMIC REFLECTORS AND RESULTS

In this section we first focus our interpretation on the interaction between magma sills emplacement sedimention, and the subsequent effects of faulting. We then address the nature of the crust-mantle boundary, to provide constraints on crustal accretion process at sedimented ridges.

Low velocity reflectors

Most of the reflections in the seismic profiles are of normal polarity as that of the seafloor reflection. However, both profiles display some reflections with reverse polarities (Figs.2A, 2B, 2C, 2D),, which suggest low velocity zones likely induced by fluids or by material with lower velocity than that of the surrounding medium.

On-axis we observe two low velocity, revese polarity reflectors. We suggest correspond to a magma bearing axial melt lens (AML), rather than other fluids such as water, as they are located below the ASSC axis; such reserve polarity reflections are commonly interpreted as the present of AMLs beneath fast spreading ridges (Detrick et al., 1987; Kent et al., 1993) and more recently at slow-spreading (Singh et al., 2006b) ridges. The shallowest one, which is 0.8 km wide at 6 s two-way travel time (TWTT) present on both profiles and we name it upper axial melt lens (U-AML). The second deeper on, which is 2-km wide at 7.2 s, is present only on profile PGS08-23 and we name it lower axial melt lens (L-AML).

We also observe some reverse polarity reflections off-axis, but owing to their position and relatively short lateral extension, they probably correspond to fluids other than magma such as water or gas circulating near faults or along sediment-sill interfaces (Fig. 2).

High velocity reflectors

Within the sedimentary layers and underneath them, we observe two sets of strong and discontinuous normal polarity reflections (Figs. 2A, 2B) that should correspond to high, positive velocity contrasts. We interpret those that are sub-horizontal (sloping < 20°) as frozen igneous bodies or sills (Figs. 2A, 2B), following similar criteria used in other studies in similar environments (Trude et al. 2003; Lizarralde et al., 2011). These reflectors tilt primarily toward the axis, where they can show a saucer-shape (Hansen and Cartwright, 2006).

Steeper reflections (>20°) can be interpreted either as highly rotated sills or as fault reflectors owing to their orientation and position in the proximity of prominent and continuous faults (Figs. 2A, 2B). We prefer to interpret them as sills because, in the sedimentary strata, faults offset sediment layers and lack any reflectivity contrast (see below). Furthermore, the high reflectivity of the frozen magma sills below the sedimentary sequence requires a surrounding medium that is not of magmatic origin.

Tectonic structures

The 600 m deep and 12-km wide axial graben is flanked by a series of high-angle (65-75º) normal faults. They have a ~1 km spacing (Figs. 2A, 2B, 3A) with a staircase pattern, dipping towards the center of the basin, and are responsible for the local subsidence. These faults are recent as they cut through the most recent sediments. The seismic profiles and the seafloor bathymetry suggest that the nature of the graben deformation and associated faulting is similar along the whole segment.

Further away from the axis and central graben, shallow-dipping (20-40º) reflections at both flanks of the median valley are shown in PGS08-21, and only on one flank for PGS08-23. In some cases, these low-angle reflectors reach deep crustal levels and show a clear tilt of the adjacent crust block. This indeed suggests a fault-related flexural rotation resulting in a shallow dip of sedimentary reflectors away from the axis. This is best shown by two of the major inward-dipping low angle Outer Bounding Fault North and South faults (OBF-N and OBF-S in Figs. 2A, 2B).

A clear bounding fault buried under more recent sediments is imaged around CMP 26000-27000 (Fig. 2A). This fault penetrates down to 700 ms above the Moho, with 500 ms thick reflective zone above the fault's lower extent (Fig. 3B). A similar, but smaller, structure is present on the conjugate side to the south. On PGS08-23, these OBFs are also visible, and have some high angle faults in a staircase pattern below them. These low-angle reflections may thus be akin to the present-day seafloor surface of the axial graben flank. The identification of high-angle, staircase patterns is increasingly difficult nearing the transform fault in the east near profile PGS08-21, where the block rotation and the deformation are the highest. Locally, we observe a sediment infill that has been tilted away from the axis, consistent with flexural rotation associated with ridgeward normal faulting. Deep-rooted low-angle faults close to the axis rupture at the seafloor. Other faults are sealed by recent sediments, forming an unconformity with the tilted blocks. Hence, the faults responsible for the tilt of these blocks are not active at the present time. This observation, together with the lack of a tectonic signal on the most recent sediment cover, lack of fault scaprs at the seafloor away from the axis, and the concentration of seismicity along the axial graben (Diehl et al., 2013), clearly demonstrate that tectonic deformation concentrates along the graben. Little or no deformation occurs off-axis, and all the tectonic

structures observed off-axis have been passively rafted due to oceanic accretion on-axis, where we focus our analysis.

Crust-Mantle boundary

The Moho reflection is generally 1-5-2.5 s into the oceanic crust (Kent et al, 1994). On our data it is imaged at ~7.6 s on profile PGS08-21 and around 7.5-7.8 s on profile PGS08-23. It is slightly shallower beneath the axial valley (Figs. 2A, 2B), and can be followed along a significant part of the profile. If the base of the sedimentary strata is the top of the oceanic crust and the Moho reflection its base, then crustal thickness would vary from 1.6 s to 2.4 s. On Profile PGS08-23, between CMP 77000 and 79000, the Moho displays a complex pattern, with lens-type structures (Figs. 2B, 3C); similar reflectors are observed near CMP 16000 and 25000 on profile PGS08-21, and around CMP 69000 and 80000 on profile PGS08-23. Beneath the spreading axis we observed a weak reflection ~ 250 ms below the L-AML, which we also interpret as the Moho.

DISCUSSION AND CONCLUSIONS

A combination of the interval P-wave velocity data and seismic reflection images of the full crustal thickness allows us to characterize for the first time with sufficient detail the nature of the whole crust formed along the axis of a sedimented spreading center.

Axial melt supply

Multiple melt lenses have been recently reported beneath fast spreading centers (Arnulf et al., 2014; Marjanovic et al., 2014), but the presence of two melt sills (U-AML and L-AML) beneath a slow spreading ridge is novel as it has been difficult to image melt lens below them (Singh et al., 2006b). Furthermore, the separation between the two melt sills is much larger (~1.2 s) than that observed at fast spreading ridge (0.2-0.3 s), and therefore, their roles should be different. The U-AML is relatively shallow when compared to the predicted depth for AMLs for the spreading rate of 3.8 cm/yr (Chen and Morgan 1990). In the absence of any enhanced melt supply to the axis, this prediction would suggest that the apparently shallow U-AML is likely a transient feature at this spreading rate, but instead the presence of the reflector on the two profiles 40-km apart indicates that the U-AML is instead a prevalent feature. This shallow melt lens position could also be facilitated by the thick sediment layer blanketing the axial valley, that likely acts as an insulating layer resulting a warmer thermal regime that could help retain a melt for longer time.

The U-AML, which lies at the base of the sedimentary cover,is also at the intersection of the median valley bounding faults, suggesting that the shallow dipping bounding faults may root at the U-AML. The U-AML is also shifted ~0.5 km northward from the axial graben on PGS08-21 and ~1.2 km on PGS08-23, inducing the southern boundary fault to dip more shallowly than the northern one. Such an asymmetry in faulting caused by the AML position has also been suggested at the Afar rift (Grandin et al., 2009).

The depth of the L-AML, at ~2.3 s below the seafloor or ~4.5 km within the igneous crust, is consistent with the prediction from lithospheric cooling models at this rpreading rate (Chen and Morgan, 1990). The L-AML likely feeds the U-AML on axis, and this magmatic system bay be

the source for other crustal melt sills near and off the spreading axis now frozen, although the the dynamics and interactions of multiple melt lenses are not well-known.

Formation of the upper crust

We identify a steep gradient in P-wave velocity ranging from 3.0 to 4.5 km/s att he base of the recent sediments, clearly associated with the numerous sills observed at this depth (Fig. S2). As for the Guyamas basin (Kluesner et al., 2014), the reflectors in this area show amplitude whitening between sills, which could be due to fluid-expulsion and metamorphism or the presence of gas (steam). The P-wave velocity in the sediments is likely to increase due to compaction and fluid expulsion, and to metamorphism around sill intrusions (Aarnes et al., 2011). Based on the P-wave velocity, we suggest that the upper crust is a 1.2 km thick velocity gradient zone composed of metamorphosed sediments and sill intrusions (Fig. 4).

Deflation due to melt extraction in the U-AML, in addition to normal faulting along the axial graben, can contribute to axial subsidence and promote the inward tilt of the sill/sediment sequences. Extension concentrated at the rift valley and its flanks would thus induce the development of steeply dipping faults (stair-case normal faults), possibly facilitating further injection of sills in the upper sedimentary strata. High-amplitude reflections below the high-velocity gradient zone are sparse, sometimes concentrating as lenses along low-angle faults. The relatively higher velocity in this crustal section is indicative of magmatic accretion, but lacking adequate velocity constrains we do not exclude it to be metamorphosed sill-sediment lenses similar in composition to the upper crust. The former interpretation would be induced by the proximity of these faults with the magma supply at the axis. The latter one would suggest high variability of the metamorphic upper crustal thickness produced by locally high subsidence, and

is more consistent with the presence of high velocity contrasts required to image these reflections.

The U-AML can define the effective brittle-ductile boundary locally while it is active, controlling the location of the inner bounding faults. After a certain amount of extension and magmatism, a new inner bounding fault would develop inward from the existing bounding faults, the older faults becoming inactive, rafted off-axis, and buried by incoming sediments. With such a process, all sill-sediment sequence now present in the graben likely forms the bulk of the upper part of the oceanic crust here. These results also suggest that the magmatic crustal accretion at the ASSC is taken up solely by intrusive processes, consistent with the absence of clear magnetic anomalies that can be attributed to eruptive units (Kamesh Raju et al., 2004), and to the lack of volcanic features along the axial graben floor. Variation in magmatic supply to the AML could be responsible for the two modes of faulting of the ASSC and would exclude the hypothesis of a halt in the oceanic crustal accretion as suggested by Morley and Alvey, (2015). On the other hand, the L-AML may locally control the rheology of the lithosphere, pinnin the root of outer bounding fault, while the two melt lenses regulate activity on the outer and inner bounding faults, and hence the nature of the median valley (Fig. 4).

Crustal thickness and Moho transition

Widespread Moho reflections allows us to constrain the nature of the lower crust and its base. Lacking accurate seismic refraction velocities, we assume a P-wave velocity of 6.8 km/s in the lower crust (e.g., Lizarralde et al., 2007). This yields a lower crustal thickness of <5.5 km, and a total crustal thickness of <6.7 km, overlain by 1.5 km of sediments, consistent with gravity-derived estimations.(Morley and Alvey (2015).

A complex Moho with lenses just above it could result from either dunite lenses (melt residue) or gabbro lenses in the mantle-crust transition zone. Frozen melt sills below the Moho have been observed beneath the Juan De Fuca Ridge (Nedimovic et al., 2005), but ASSC lenses seem to lie within the Moho transition zone, and could be the residue of former L-AMLs. The complex Moho transition zone with dunite-gabbro lenses observed in the Oman ophiolite (Braun and Kelemen, 2002) may be a suitable analog to the complex Moho we image here. The proximity of the Moho with lower melt lens creates a complex mantle transition zone, which combined with the presence of multiple sills, makes the sedimented ridge a special class of ocean spreading center forming unique marginal crust, but accurate seismic velocities are required to estimate the magmatic supply to the axis from the relative proportion of sediment and magma and its variation in depth.

ACKNOWLEDGMENTS

We would like to thank Petroleum Geo-Services (PGS) for providing the data, and Adrien Arnulf and Wayne Crawford for discussions.

REFERENCES CITED

Aarnes, I., Fristad, K., Planke, S., and Svensen, H., 2011, The impact of host-rock composition on devolatilization of sedimentary rocks during contact metamorphism around mafic sheet intrusions: Geochemistry, Geophysics, Geosystems, v. 12, no. 10, Q10019, doi:10.1029/2011GC003636.

Arnulf, A. F., Singh S. C., and Pye J. W., 2014, Seismic evidence of a complex multi-lens melt reservoir beneath the 9° N Overlapping Spreading Center at the East Pacific Rise: Geophysical Research Letters, v. 41, p. 6109-6115.

Braun, M. G., and Kelemen, P.B., 2002, Dunite distribution in the Oman ophiolite: Implications for melt flux through porous dunite conduits: Geochemistry, Geophysics, Geosystems, v. 3, no. 11, Q8603, DOI: 10.1029/2001GC000289.

Buck, W. R., Lavier, L. L., and Poliakov, A. N. B., 2005, Modes of faulting at mid-ocean ridges: Nature, v. 434, p. 719-723.

Bruvoll, V., Breivik, A. J., Mjelde, R., and Pedersen, R., B., 2009, Burial of the Mohn-Knipovich seafloor spreading ridge by the Bear Island Fan: Time constraints on tectonic evolution from seismic stratigraphy: Tectonics, v. 28, no. TC4001, DOI: 10.1029/2008TC002396.

Chen, Y., and Morgan, W. J., 1990, A Nonlinear Rheology Model for Mid-Ocean Ridge Axis Topography: Journal of Geophysical Research, v. 95, p. 17583-17604.

Curray, J. R., Moore, D. G., Lawver, L. A., Emmel, F. J., Raitt. R. W., Henry, M., and Kieckhefer, R., 1979, Tectonics of Andaman Sea and Burma, *in* J. S. Watkins, L. Montadert and P. W. Dickerson, eds, Geological and Geophysical Investigations of Continental Margins edited by: American Association Petrology Geology, Memoir 29, p. 189–198.

Davis, E.E., and Becker, K., 2002, Observations of natural-state fluid pressures and temperatures in young oceanic crust and inferences regarding hydrothermal circulation: Earth and Planetary Science Letters, v. 204, p. 231-248.

Detrick, R. S, Buhl, P., Vera, E., Mutter, J., Orcutt, J., Madsen, J., and Brocher, T., 1987, Multi-

channel seismic imaging of a crustal magma chamber along the East Pacific Rise: Nature, v. 326, p. 35-41.

Diehl, T., Waldhauser, F., Cochran, J. R., Kamesh Raju, K. A., Seeber, L., Schaff, D., and Engdahl, 2013, Back-arc extension in the Andaman Sea: Tectonic and magmatic processes imaged by high-precision teleseismic double-difference earthquake relocation: Journal of Geophysical Research: Solid Earth, v. 118, p. 1-19.

Fitch, T. J., 1972, Plate convergence, Transcurrent Faults, and Internal Deformation Adjacent to Southeast Asia and the Western Pacific: Journal of Geophysical Research, v. 77, p. 4432-4460.

Grandin, R., et al., 2009, September 2005 Manda Hararo-Dabbahu rifting event Afar (Ethiopia) : Constraints provided by geodetic data : Journal of Geophysical Research, v. 114, no. B08404, DOI: 10.1029/2008JB005843.

Hansen, D., M., and Cartwright, J., 2006, The three-dimensional geometry and growth of forced folds above saucer-shaped igneous sills: Journal of Structural Geology, v. 28, p. 1520-1535.

Kamesh Raju, K. A., Ramprasad, T., Rao, P. S., Ramalingeswara Rao, B., and Varghese, J., 2004, New insights into the tectonic evolution of the Andaman basin, northeast Indian Ocean: Earth and Planetary Science Letters, v. 221, p. 145-162.

Kent, G. M., Harding, A. J., Orcutt, J. A., 1993, Distribution of Magma Beneath the East Pacific Rise Between the Clipperton Transform and the 9°17'N Deval From Forward Modeling of Common Depth Point Data: Journal of Geophysical Research, v. 98, p. 13945-13969.

Kent, G. M., Harding, A. J., Orcutt, J. A., Detrick, R. S., Mutter, J. C., Buhl, P., 1994, Uniform accretion of oceanic-crust south of the Garrett transform at 14-degrees-15's on the East

Pacific Rise: Journal of Geophysical Research-Solid Earth, v. 99, p. 9097-9116.

Kluesner, J., Lonsdale, P., and González-Fernández, A., 2014, Late Pleistocene cyclicity of sedimentation and spreading-center structure in the Central Gulf of California: Marine Geology, v. 347, p. 58-68.

Lizarralde, D., et al., 2007, Variation in styles of rifting in the Gulf of California: Nature, v. 448, p. 466-469.

Lizarralde, D., Adam Soule, S., Seewald, J. S., Proskurowski, G., 2011, Carbon release by off-axis magmatism in a young sedimented spreading centre: Nature Geoscience, v. 4, p. 50–54.

Marjanović, M., Carbotte, S. M., Carton, H., Nedimović, M. R., Mutter J. C., and Canales, J. P., 2014, A multi-sill magma plumbing system beneath the axis of the East Pacific Rise: Nature Geoscience, v. 7, p. 825-829.

Morley, C.K., and Alvey, A., 2015, Is spreading prolonged, episodic or incipient in the Andaman Sea? Evidence from deepwater sedimentation: Journal of Asian Earth Sciences, v. 98, p. 446-456.

Nedimović, M. R., Carbotte, S. M., Harding, A. J., Detrick, R. S., Pablo Canales, J., Diebold, J. B., Kent, G. M., Tischer, M., and Babcock, M. J., 2005, Frozen magma lenses below the oceanic crust: Nature, v. 436, p. 1149-1152.

Needham, H. D., and Francheteau, J., 1974, Some characteristics of the rift valley in the Atlantic ocean near 36°48’ North: Earth and Planetary Science Letters, v. 22, p. 29–43.

Sieh, K., and Natawidjaja, D., 2000, Neotectonics of the Sumatran fault, Indonesia: Journal of Geophysical Research, v. 105, p. 28295-28326.

Singh S. C., et al., 2006b, Discovery of a magma chamber and faults beneath a Mid-Atlantic

Ridge hydrothermal field: Nature, v. 442, p. 1029-1032.

Smith, W. H. F., and Sandwell, D. T., 1997, Global sea floor topography from satellite altimetry and ship depth sounding: Science, v. 227, p. 1956-1962.

Trude, J., Cartwright, J., Davies, R., J., and Smallwood, J., 2003, New technique for dating igneous sills: Geology, v. 31, no. 9, p. 813-816.

FIGURE CAPTIONS

Figure 1: **Andaman Sea Spreading Centre**: A: General map of the study area (Multibeam bathymetry from Kamesh Raju et al., 2004 added to the bathymetry of Smith and Sandwell, 1997). ANF: Andaman Nicobar Fault, SFS: Sumatra Fault System. Red line: Andaman Sea Spreading Centre (ASSC). ATF: Andaman Transform Fault. Black box indicates area shown in Figure 1b. Arrows indicate the sense of the movement. B: Detailed map of the Andaman Sea spreading center. Black lines indicate normal faults. The red lines indicate the seismic lines shown in this study.

Figure 2: **Seismic profiles**: Interpreted seismic images A: PGS08-21 and B: PGS08-23. Time here is a two-way travel time. The black dashed box refers to Figure 3A. The black boxes mark the images shown in Figures 3B and 3C. CMP: Common Mid-Point. Blue horizons indicate the seafloor. Active faults are indicated by black lines and inactive by dashed black lines. Sills are highlighted by orange lines, possible hydrothermal deposits by dark blue lines, possible fluids by light blue lines and the Moho by pink lines. The dashed pink lines indicate the top of the reflective zone above the Moho. Green lines highlight some horizons in the sediments, variations

in the green color is made to differentiate the sedimentary units. Red lines mark melt lenses. U-AML: Upper Axial Melt Lens and L-AML: Lower Axial Melt Lens. The dark boxes mark the images shown in C and D. C: Seafloor fattened image beneath valley floor for profile PGS08-21. Small black boxes indicate polarity plots, from top to bottom: Polarity of the seafloor, polarity of a sill, and polarity of the U-AML. D: Seismic image with L-AML flatten. Small black boxes indicate polarity plots, from top to bottom: polarity of a sill near the seafloor, complex area with no clear polarity, polarity of the U-AML, polarity of the L-AML.

Figure 3**: Expanded view of seismic data:** Interpretation uses the same colors as figure 2. A: Depth converted seismic image in the median valley along profile PGS08-21. The velocity model used is the one in supplementary Figure S2. The thickness of the faults is proportional to the offset they induce. B: Time (not depth converted) blow-up of seismic image of a buried bounding fault and associated sills, C: Time (not depth converted) blow-up of a reflective zone above the Moho.

Figure 4: **Crustal model of sedimented ASSC**: Schematic 3D block diagram synthesizing different features observed along both profiles. The block diagram differentiates un-metamorphosed sedimentary layers in green, yellow and white, upper crust in light brown, lower crust in brown, mantle transition zone in purple and mantle in pink. The blue line shows the position of the 1.5, 3.0 and 4.5 km/s velocity limit (from figure S2). On the right, a diagram proposes the respective proportions of the sediments versus the igneous material.

Figure S1: **Un-interpreted seismic images:** A: Profile PGS08-21. B: Profile PGS08-23.

Figure S2: **Interval Velocity:** Interval velocity as a function of time derived from the root mean square velocity superimposed on the interpreted profile PGS08-21 (Fig. 2A).

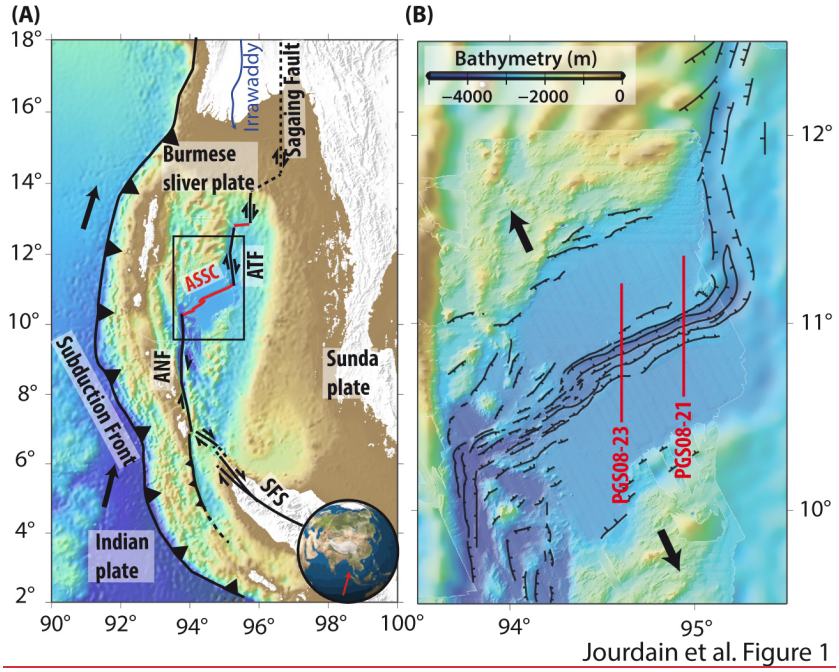

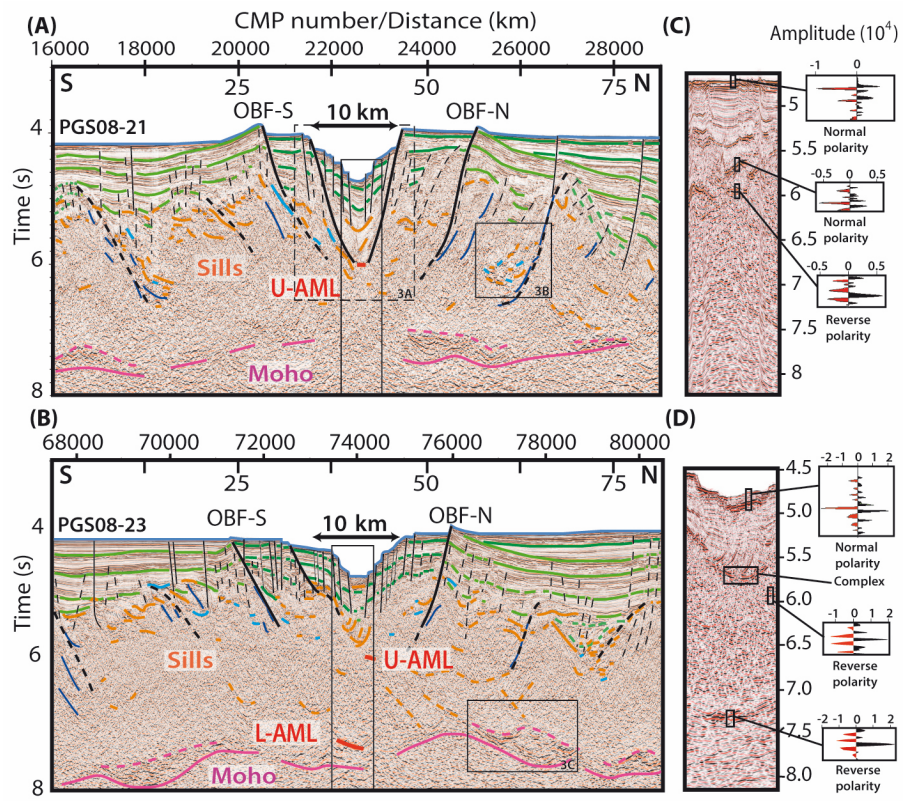

Jourdain et al. Figure 2

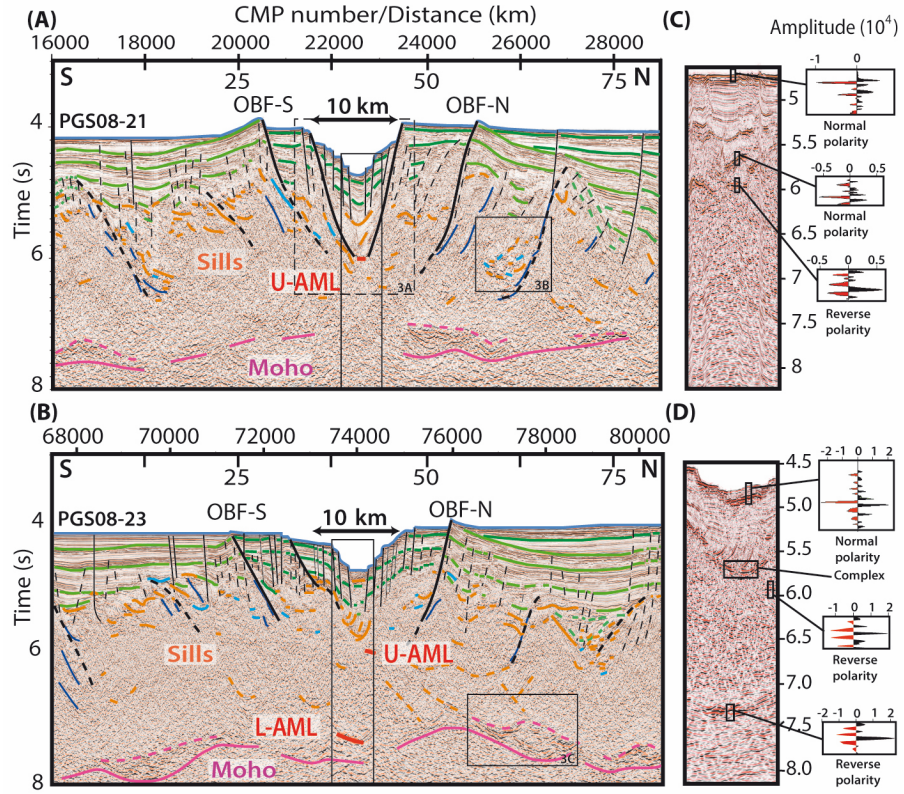

Jourdain et al. Figure 2

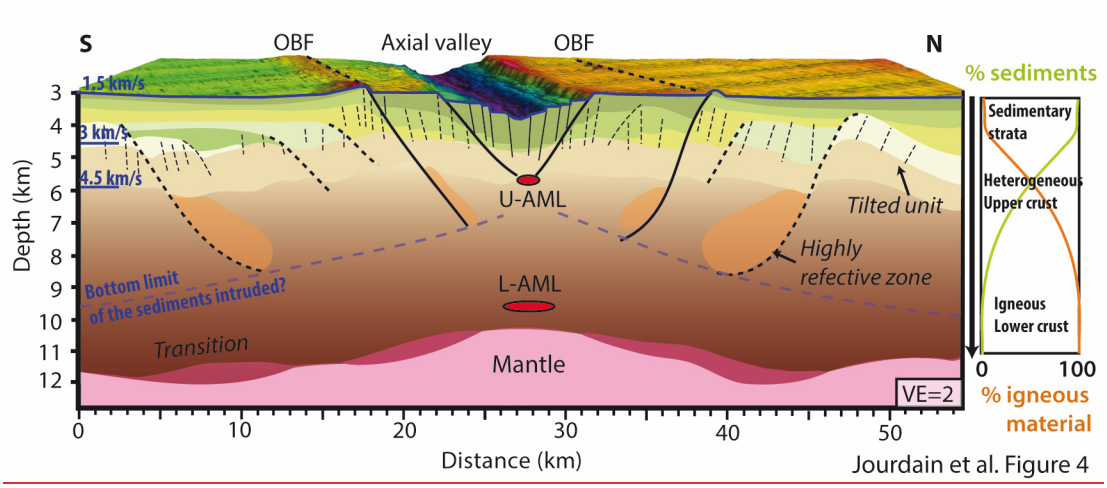

Jourdain et al. Figure 4

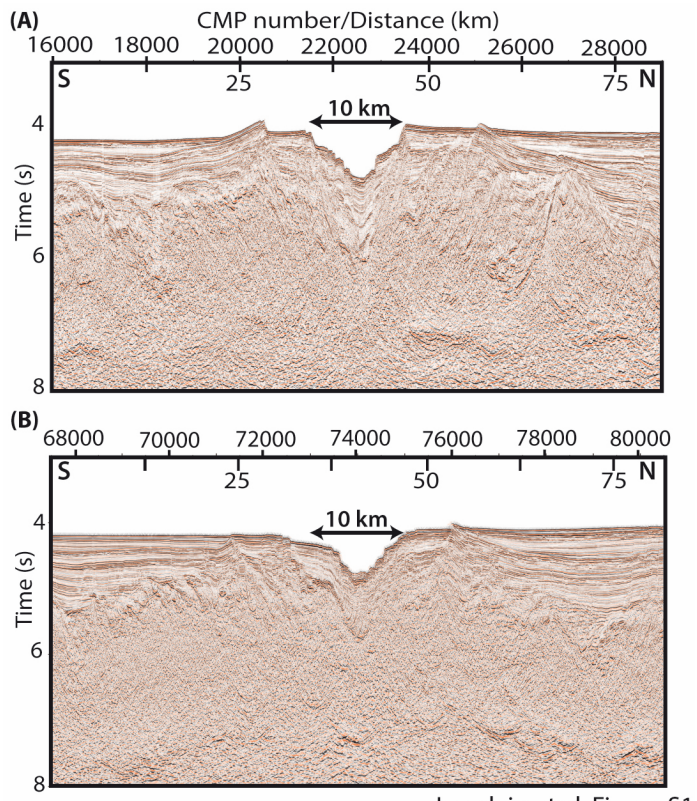

Jourdain et al. Figure S1

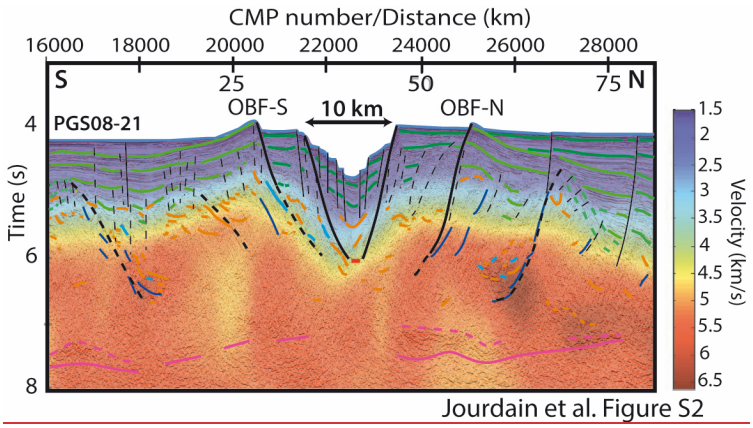

Jourdain et al. Figure S2